PAPER • OPEN ACCESS

Understanding hydrogen and heat diffusion across c–Si/a–Si:H heterojunctions for improved thermal management in solar cells fabrication

To cite this article: Riccardo Dettori *et al* 2025 *Nanotechnology* **36** 155703

View the article online for updates and enhancements.

You may also like

- Simultaneous Reduction of Radiation Dose and Scatter-to-Primary Ratio using a Truncated Detector and Advanced Algorithms for Dedicated Cone-Beam Breast CT
HSIN WU TSENG, Srinivasan Vedantham and Zhiyang Fu

- Role of anisotropic confining potential and elliptical driving in dynamics of a Ge hole qubit
Bashab Dey and John Schliemann

- Ionically gated transistors based on two-dimensional materials for neuromorphic computing
Susan Fullerton-Shirey and Ke Xu

EDINBURGH INSTRUMENTS
SCAN ME
RMS1000 MULTIMODAL CONFOCAL MICROSCOPY
Raman
Photoluminescence
Second Harmonic Generation
Fluorescence & Phosphorescence Lifetime
VISIT OUR WEBSITE FOR MORE DETAILS
MADE IN THE UK
edinst.com

This content was downloaded from IP address 192.84.153.4 on 05/03/2025 at 12:49

OPEN ACCESS
IOP Publishing

Nanotechnology

Nanotechnology **36** (2025) 155703 (14pp)

https://doi.org/10.1088/1361-6528/adb8f3

Understanding hydrogen and heat diffusion across c–Si/a–Si:H heterojunctions for improved thermal management in solar cells fabrication

Riccardo Dettori*, Claudio Melis and Luciano Colombo

Department of Physics, University of Cagliari, Monserrato, CA 09042, Italy

E-mail: riccardo.dettori@dsf.unica.it

Received 3 January 2025, revised 31 January 2025
Accepted for publication 21 February 2025
Published 5 March 2025

Abstract

c-Si/a-Si:H-based solar cells are characterized by impressive efficiencies for silicon based devices. In this paper, we present a comprehensive atomistic simulation study of the structural and transport properties of crystalline silicon and hydrogenated amorphous silicon heterostructures for photovoltaic applications. By leveraging state-of-the-art molecular dynamics simulations with a machine-learned force field, we explore the effects of thermal boundary resistance as well as hydrogen diffusion on device performance. The simulations reveal the dependence of thermal properties on crystalline orientations, cooling rates of the amorphous layer, and interface morphology. A systematic investigation of hydrogen diffusion demonstrates its impact on heat transport and structural stability, highlighting the role of moderate hydrogenation ($\leqslant$10%) and specific orientations in enhancing thermal dissipation and reducing degradation. These findings provide atomistic insights into optimizing c-Si/a-Si:H interfaces, enabling improved thermal management and long-term stability for high-performance solar cells.

Keywords: silicon, solar cell, heterostructures, molecular dynamics

1. Introduction

The rapid development of silicon-based photovoltaic (PV) technologies over the past few decades has been driven by the pursuit of higher conversion efficiencies, lower manufacturing costs, and improved device stability. Among the most promising device architectures are heterojunction (HJ) solar cells, that integrate crystalline silicon (c–Si) wafers with thin layers of hydrogenated amorphous silicon (a–Si:H). These HJ devices have achieved globally leading performances, exceeding 25% efficiency and nearing the upper limit of 26% [1, 2]. Central to this achievement is the exceptional ability of a-Si:H to provide high-quality surface passivation at the c-Si interface.

A key advantage of c–Si/a–Si:H HJs lies in the capacity of the hydrogen-rich amorphous silicon layer to electronically passivate the c–Si surface, minimize dangling bonds, and mitigate interface defect densities [3–5]. This enhanced passivation prolongs the carrier lifetimes and raises V_{OC} [2, 6]. Additionally, doped a–Si:H layers facilitate the formation of effective emitter and back-surface field regions [6, 7], enabling optimal band bending and charge transport at both the front

* Author to whom any correspondence should be addressed.

Original Content from this work may be used under the terms of the Creative Commons Attribution 4.0 licence. Any further distribution of this work must maintain attribution to the author(s) and the title of the work, journal citation and DOI.

© 2025 The Author(s). Published by IOP Publishing Ltd

and rear interfaces. Furthermore, the relatively low processing temperatures required for HJ device fabrication make these technologies compatible with high-throughput, cost-effective manufacturing, effectively reducing both production complexity and energy payback times compared to the conventional high-temperature diffusion processes employed in standard c–Si solar cells [7–9].

Despite these notable achievements, the efficiency of current devices remains below the theoretical Shockley–Queisser limit (33%–35% [10]) prompting continued research efforts to enhance performance. Key challenges include obtaining ideal atomic-scale architecture of c–Si/a–Si:H interface, optimizing doping profiles within the thin amorphous layers, and ensuring long-term device stability under operational conditions [6, 11–13]. A central obstacle lies in refining and stabilizing the c–Si/a–Si:H interface. Residual dangling bonds and subtle variations in hydrogen content, chemical composition, and local atomic ordering can introduce mid-gap states that act as recombination centers [14, 15]. Besides the challenges posed by doping optimization in a–Si:H layers (e.g. defect formation, increased recombination, dopant trapped in inactive configurations)[16, 17] [?], the long-term stability of these devices under realistic operating conditions remains a significant concern, as factors such as illumination, temperature fluctuations, and mechanical stress can induce structural rearrangements, hydrogen diffusion, and the formation or reactivation of defects, gradually affecting performance [18–20]. A major limitation in advancing c–Si/a–Si:H HJ solar cells is the incomplete understanding of the microscopic conditions at the c–Si/a–Si:H interface, both immediately after deposition and throughout annealing processes [21–26].

A critical factor that has recently attracted attention is the thermal boundary resistance (TBR) at the c–Si/a–Si:H interface [27–29]. Although these interfaces are primarily designed for electronic optimization, thermal transport across material boundaries can significantly affect the device reliability and stability. A larger TBR might increase localized heating and enhance the temperature gradient across the heterostructure interface. This can accelerate defect formation, enhance undesirable diffusion processes, and ultimately influence the lifetime and efficiency of the solar cell [30, 31]. For instance, increased TBR can promote the formation or reactivation of interface states by elevating local temperatures during device operation or under intense sunlight, thereby affecting passivation quality. Understanding and minimizing TBR is therefore crucial to mitigate thermal-related degradation pathways, especially as cell architectures become more complex and push toward higher power densities [27, 29]. Furthermore, hydrogen diffusion remains a persistent and multifaceted challenge in c–Si/a–Si:H heterostructures [32, 33]. Although hydrogen incorporation is central to achieving high-quality passivation in the amorphous layer, hydrogen atoms can also become mobile under thermal or electrical stress. This diffusion can degrade passivation over time by leaving behind dangling bonds or by clustering at defect sites. Such processes negatively influence carrier lifetimes and device reliability, and the difficulty of directly observing hydrogen diffusion in real time further complicates the problem [32]. Consequently, both TBR-related thermal effects and hydrogen migration strongly couple to interface passivation quality—factors that ultimately dictate the cell performance and durability.

In this context, theoretical and computational methods present valuable opportunities to overcome existing knowledge gaps and advance the design of HJ solar cells [34]. A multi-scale framework is necessary to achieve further performance gains. Specifically, predicting how atomic-scale modifications—such as the targeted introduction of hydrogen, changes in dopant profiles, or thermal annealing procedures—ultimately affect device-level figures of merit. Atomistic simulations can help bridging this gap. Molecular dynamics (MDs) approaches, especially those guided by first-principles methods based on density functional theory (DFT), have become increasingly potent in accurately modeling the structural and dynamic properties of amorphous networks and their interfaces with crystalline substrates [35–38]. These computational tools enable the detailed exploration of atomic-level processes governing defect generation, hydrogen diffusion and passivation, dopant incorporation, and the consequent effects on the electronic structure, thereby contributing to a deeper understanding of HJ solar cell behavior. Nonetheless, standard DFT approaches suffer from unfavorable computational scaling—on the order of $\mathcal{O}(N^3)$—due to the requirement of solving for Kohn–Sham eigenstates, thus constraining DFT-based MD simulations to relatively modest system sizes (few hundreds of atoms) and short timescales (tens of picoseconds) in many cases. In this regard, machine-learning-driven methodologies for building interatomic potentials have gained traction for modeling both reactive and nonreactive materials [39, 40]. Among these, Gaussian process regression in the form of the Gaussian approximation potential (GAP) has been applied to a range of materials systems, including silicon-based networks [41]. Such potentials can achieve near *ab initio* accuracy at substantially reduced computational cost, enabling the exploration of larger system sizes or longer time windows. Indeed, GAP has previously been employed to investigate c–Si/a–Si:H HJ [32], although the large number of fitting parameters can limit both the accessible system size and simulation duration. Moreover, the construction of these potentials remains labor-intensive, as machine learning models typically demand extensive training datasets [40] and can be susceptible to overfitting [42]. In addition, the high dimensionality of parameter space often results in a more computationally intensive workload compared to classical force-field MD simulations. A viable alternative is the Chebyshev interaction model for efficient simulation (ChIMES) [43–45], which leverages a linear expansion in Chebyshev polynomials to reproduce atomic forces and energies in both molecular and condensed-phase systems with comparatively lower data demands. ChIMES has been successfully employed in modeling non-reactive and reactive systems alike, such as water under ambient and high-pressure conditions [46, 47], high-pressure C/O materials [45, 48], and detonating energetic compounds [49].

In this work, we employ the ChIMES force field to model silicon-hydrogen interactions in c–Si/a–Si:H HJs. Through a

systematic MD study, we explore both the thermal properties of the HJ interface and hydrogen diffusion pathways, revealing possible correlations between structural features and transport mechanisms. Our findings provide valuable insights for mitigating device degradation and enhancing overall performance in c–Si/a–Si:H HJ.

The paper is organized as follows. First, we describe the computational framework used to develop the Si–H force field, emphasizing key details in the generation of the ChIMES potential. We then outline the protocol for constructing the HJ samples, with particular attention to the preparation of the amorphous silicon component. Finally, we present our results on the c–Si/a–Si TBR, analyzed as an autonomous thermodynamic system, and hydrogen diffusion behavior in the HJ, two factors that could significantly influence device performance.

2. Methods

Below, we provide a concise description of the core formalism underlying the ChIMES force field, which has been extensively explained elsewhere [43, 45, 50, 51]. We focus here on the key expressions and relevant parameters as they pertain to the current work.

Starting from a many-body expansion of the total energy, the DFT reference energy of the system can be written as

$$E_{\mathrm{DFT}} = \sum_{i_1}^{n_a} E_{i_1}^{1B} + \sum_{i_1>i_2}^{n_a} E_{i_1 i_2}^{2B} + \sum_{i_1>i_2>i_3}^{n_a} E_{i_1 i_2 i_3}^{3B} + \sum_{i_1>i_2>i_3>i_4}^{n_a} E_{i_1 i_2 i_3 i_4}^{4B} + \cdots + \sum_{i_1>i_2\ldots\, i_{n_B-1}>i_{n_B}}^{n_a} E_{i_1 i_2 \ldots i_n B}^{nB}. \quad (1)$$

Here, n_a is the total number of atoms in the system, and the many-body expansion extends from one-body ($1B$) energies, $E_{i_1}^{1B}$, which correspond to the atomic energy constants, to two-body ($2B$) pairwise interactions, $E_{i_1 i_2}^{2B}$, and so on, up to the maximum number of bodies n_B.

In ChIMES, each term in the many-body expansion is represented via a linear combination of Chebyshev polynomials of the first kind, $T_m(x)$, where $x = \cos\theta$. For example, the two-body term takes the form

$$E_{ij}^{2B} = f_p(r_{ij}) + f_c(r_{ij}) \sum_{n=1}^{N_{2B}} C_n T_n(x_{ij}) \quad (2)$$

where C_n is the permutationally invariant coefficient for the atomic pair i,j and $T_n(x_{ij})$ represents a Chebyshev polynomial of order n. The variable $x_{ij} = S(r_{ij})$ is derived from a Morse-like transformation [45, 52, 53] that maps the interatomic distance r_{ij} to the interval $[-1, 1]$ (i.e. the domain of Chebyshev polynomials). Specifically, $S(r_{ij})$ is proportional to $\exp(-r_{ij}/\lambda)$, with λ defined as the interatomic distance of the maximum in the first peak of the pair correlation function. The function $f_c(r_{ij})$ is a Tersoff-type cutoff [54], which smoothly goes to zero beyond a specified distance for a given atom pair. To avoid sampling interatomic separations outside the range provided by the training data, a smooth penalty function $f_p(r_{ij})$ is also included.

Extending beyond the two-body term, higher-order contributions are generated by defining clusters of size n and taking the product of the corresponding two-body polynomials from the $\binom{n}{2}$ unique pairs in that cluster. For instance, the three-body term involves products of the three unique pair interactions for atoms i,j,k, leading to

$$E_{ijk}^{3B} = f_c(r_{ij}) f_c(r_{ik}) f_c(r_{jk}) \sum_{r=1}^{N_{3B}} \sum_{s=1}^{N_{3B}} \sum_{t=1}^{N_{3B}} C_{rst} T_r(x_{ij}) T_s(x_{ik}) T_t(x_{jk}) \quad (3)$$

where C_{rst} is the permutationally invariant coefficient for the triplet i,j,k. As in the two-body case, the f_c functions define distance cutoffs for each interatomic distance in the triplet. Penalty functions remain confined to the two-body interactions, ensuring computational efficiency.

ChIMES can be systematically extended to even higher-bodied interactions in a similar manner. Additional details regarding its methodology and implementation can be found in the literature [49]. Optimal ChIMES parameters (the coefficients of linear combination) can then readily be determined by minimizing the objective function

$$F_{\mathrm{obj}} = \sqrt{\frac{1}{N_d} \times \left(\sum_{\tau=1}^{M} \sum_{i=1}^{N} \sum_{\alpha=1}^{3} w_{F_{\alpha_i}}^2 (\Delta F_{\alpha_i})^2 + \sum_{\tau=1}^{M} \sum_{\alpha=1}^{3} w_{\sigma_{\alpha\alpha}}^2 (\Delta\sigma_{\alpha\alpha})^2 + \sum_{\tau=1}^{M} w_E^2 (\Delta E)^2 \right)}, \quad (4)$$

where M is the total number of configurations in the training set and N_d is the total number of data entries ($3MN$ force components plus $3M$ stress tensor components plus M energy components). In addition, $\Delta F_{\alpha_i} = F_{\mathrm{ChIMES}_{\alpha_i}}^{\tau} - F_{\mathrm{DFT}_{\alpha_i}}^{\tau}$, $\Delta\sigma_{\alpha\beta} = \sigma_{\mathrm{ChIMES}_{\alpha\beta}}^{\tau} - \sigma_{\mathrm{DFT}_{\alpha\beta}}^{\tau}$, and $\Delta E_i = E_{\mathrm{ChIMES}}^{\tau} - E_{\mathrm{DFT}}^{\tau}$. In what follows, we derived our force field by only fitting the atomic forces and the stress tensor components, thus omitting the term ΔE

To prepare our training dataset, we began with an existing set originally developed to capture the silicon repulsive energy for density functional tight-binding simulations [50]. This dataset contains DFT-MD snapshots of several silicon phases: a diamond-structure supercell of 64 atoms, a body-centered cubic supercell of 54 atoms, a simple cubic cell of 64 atoms, and a graphene-like sheet of 32 atoms. The training set also includes uniformly expanded and contracted versions

of the diamond and graphene supercells, spanning 90%–110% of their ground-state densities. The variety of structures in the training set enables the ChIMES cluster expansion approach to capture the local environment of silicon atoms with high accuracy and ensures transferability across multiple silicon polymorphs, including reliable predictions of vibrational spectra. Each MD simulation was conducted for approximately 5 ps at 600 K, with snapshots collected every 200 fs, yielding a total of 838 configurations for the ChIMES force-field development. This broad sampling range is designed to capture diverse bonding environments and interatomic interactions characteristic of amorphous silicon. For our specific objectives, we augmented this dataset with an additional 89 configurations of liquid silicon at 2000 K, plus 58, 21 and 100 frames respectively of silane (SiH_4), silicon dihydride (SiH_2), and silicon hydride (SiH) at 200 and 300 K. All DFT calculations were carried out using the Vienna *ab initio* simulation package [55], employing projector-augmented wave pseudopotentials [56, 57] and the Perdew–Burke–Ernzerhof exchange-correlation functional [58]. A plane-wave cutoff of 500 eV was found to sufficiently converge our results and was used throughout. We adopted an electronic convergence threshold of 10^{-6} eV, along with a force convergence criterion of 10^{-2} eV Å^{-1} during all structural optimizations. The Mermin functional [59] smearing was set to 0.03 eV in all calculations. To ensure accurate energy and pressure estimations, we sampled the Brillouin zone using a $2 \times 2 \times 2$ Monkhorst–Pack **k**-mesh [60] for the supercells described above.

The linearity of the ChIMES potential on its fitting coefficients allows the implementation of robust global optimization techniques that are otherwise inaccessible to non-linear machine-learning models. For this work, we employed least-angle regression with least absolute selection and shrinkage operator regularization [62–64], using a regularization parameter $\alpha = 10^{-3}$. Given the short-ranged character of silicon–silicon interactions and our focus on hydrogen interstitial adsorption and diffusion, we sampled interatomic distances within 2.0–4.0/5.0 Å for Si–Si pairs, 1.0–4.0/5.0 Å for Si–H pairs, and 0.5–1.5 Å for H–H pairs. We then tested the ChIMES force field with different polynomial orders for the two-body (N_{2B}), three-body (N_{3B}), and four-body (N_{4B}) terms. All force field validations and production runs were performed using LAMMPS [65], employing a timestep of 1 fs for simulations involving only silicon, and 0.5 fs for those containing hydrogen. All our simulations were performed with periodic boundary conditions in all directions, except the non-equilibrium runs to calculate the TBR in which we fixed the simulation cell along the transport direction x.

Table 1 compares the computed bulk silicon lattice constants for several variants of our ChIMES force field against those obtained with the Tersoff potential [54], the GAP potential [61] and *ab initio* calculations. The last column presents the percentage deviation from the *ab initio* lattice parameter. It is evident that considering the four-body interactions helps improving the stability of the force field. Furthermore, increasing the polynomial order tends to produce better agreement overall, albeit the improvement is not striking. In fact, overly high polynomial orders can lead to overfitting, consequently degrading predictive performance. Furthermore, expanding the sampled interatomic distance range appears to better capture the experimentally observed lattice parameter.

Table 1. ChIMES calculated bulk silicon lattice constants for different polynomial orders and r_{max}.

N_{2B}—N_{3B}—N_{4B}	$r_{max}^{Si-Si/Si-H}$ (Å)	a (Å)	
8–4–0	4	5.506	0.7%
	5	5.549	1.5%
8–4–2	4	5.504	0.6%
	5	5.551	1.5%
12–8–0	4	5.499	0.6%
	5	5.451	−0.3%
12–8–4	4	5.449	−0.4%
	5	5.476	0.1%
16–12–0	4	5.492	0.4%
	5	5.440	−0.5%
16–12–4	4	5.449	−0.4%
	5	5.456	−0.2%
20–16–0	4	5.491	0.4%
	5	5.454	−0.3%
Tersoff		5.431	−0.7%
GAP [61]		5.460	−0.1%
DFT (Si)		5.469	

To assess the accuracy of the Si–H interactions, we computed the lattice constants for solid SiH_4, which has a melting point of ~ 88 K and a boiling point of ~ 188 K (both of which lie well below the temperatures of the configurations employed in our training set). This compound crystallizes in the monoclinic $P2_1/c$ space group: in table 2, we report the a and b lattice constants, as well as the lattice angle β between the a and c axes (given that α and γ were 90° in both the DFT-based simulation cell and the test performed with the ChIMES force field). The deviation with respect to the *ab initio* values is larger compared to bulk silicon, but some combinations of N_{2B}—N_{3B}—N_{4B} (e.g. 12–8–0 with $r_{max}^{Si-Si/Si-H} = 5.0$ Å) results in very good agreement of both lattice constant and cell angle. Hence, increased polynomial complexity does not necessarily translate into improved results, and four-body interactions do not markedly enhance the modeling of Si–H interactions.

It is worth noting that our training set included Si–H-bearing molecules only in their gas-phase configuration, so the agreement observed here is quite encouraging. Moreover, for this study, the main focus is on interstitial hydrogen in crystalline silicon, which places less stringent demands on reproducing accurate SiH_4 lattice parameters. Based on these preliminary findings, we identified the optimal potential by

Table 2. ChIMES calculated SiH_4 lattice constants for different polynomial orders and different cutoff distances $r_{max}^{Si-Si/Si-H}$.

N_{2B}–N_{3B}–N_{4B}	$r_{max}^{Si-Si/Si-H}$ (Å)	a (Å)		b (Å)		β (°)	
8–4–0	4.0	7.558	−8.5%	4.970	−8.5%	95.2	8.5%
	5.0	7.912	−13.6%	5.204	−13.6%	89.9	13.6%
8–4–2	4.0	7.508	−7.8%	4.938	−7.8%	96.0	7.8%
	5.0	7.046	−1.2%	4.634	−1.2%	102.8	1.2%
12–8–0	4.0	7.613	−9.3%	5.007	−9.3%	94.4	9.3%
	5.0	6.795	2.4%	4.469	2.4%	101.6	2.4%
12–8–4	4.0	8.115	−16.5%	5.337	−16.5%	86.9	16.5%
	5.0	7.773	−11.6%	5.112	−11.6%	92.0	11.6%
16–12–0	4.0	7.701	−10.6%	5.065	−10.6%	93.0	10.6%
	5.0	7.856	−12.8%	5.166	−12.8%	90.8	12.8%
16–12–4	4.0	8.725	−25.3%	5.738	−25.3%	77.7	25.3%
	5.0	10.841	−55.7%	7.130	−55.7%	46.1	55.7%
20–16–0	4.0	8.762	−25.8%	5.762	−25.8%	77.2	25.8%
	5.0	7.128	−2.3%	4.688	−2.3%	101.7	2.3%
DFT		6.965		4.581		104.1	

employing a cutoff distance of $r_{max}^{Si-Si/Si-H} = 5.0$ Å for both Si–Si and Si–H interactions, enabling us to narrow down the final candidates for further investigations.

We next evaluated various force field candidates by examining key structural properties of crystalline and amorphous silicon. In view of the large parameter space, we report here only our final selection to streamline the discussion. Because adding more parameters inevitably increases the computational overhead, we restricted our choice to the following configuration: $N_{2B} = 12$, $N_{3B} = 8$, $N_{4B} = 0$ and $r_{max}^{Si-Si/Si-H} = 5.0$ Å. In figure 1, we report a comparison of the Si–Si radial distribution function $g(r)$, the Si–Si–Si angle distribution function $d(\alpha)$, and the distribution of the average coordination number for crystalline and liquid silicon at T = 2000 K. Our results show an excellent agreement of $g(r)$ for both c–Si and liquid Si, resulting in a more structured second and third coordination shell compared to the Tersoff prediction, which instead fails in accurately describing the short and medium range structure of both phases (figures 1(a) and (c)). As for the $d(\alpha)$, ChIMES predicts a slightly lower and broader distribution of the angles in c-Si, but correctly represents the angle distribution of the liquid phase, while Tersoff fails in describing both (figures 1(c) and (e)). These features reflect in a very accurate description of the amorphous network also in terms of number of neighbors (figure 1(f)).

We further tested the force field performance in describing hydrogen diffusion through interstitial sites of both crystalline and amorphous silicon. Previous studies, using tight-binding and first-principles calculations, have shown that hydrogen diffusion in c–Si proceeds via jumps between non-nearest-neighbor bond-center sites, leading to deviations from standard Arrhenius-like high-temperature behavior [66, 67]. Figure 2 presents our calculated hydrogen diffusion in c–Si and a–Si over the temperature range $600 \leqslant T \leqslant 1800$. Our model correctly predicts its order-of-magnitude 10^4 cm^2 s^{-1} for $T > 1000$ K [66], somewhat overestimating its actual value for lower temperatures; this is likely to be attributed to the presence of covalent Si–H configurations in the training set. In terms of force-accuracy, our final ChIMES candidate ($N_{2B} = 12$, $N_{3B} = 8$, $N_{4B} = 0$ and $r_{rmmax}^{Si-Si/Si-H} = 5.0$ Å) exhibits a force error of 0.22 eV Å^{-1} for Si and 0.28 eV Å^{-1} for H, which is comparable with the reported Si–H GAP error [68] (0.13 and 0.22 eV Å^{-1}, respectively). We note that further increasing the polynomial order and the bodiedness in ChIMES could lower this error, although at believe expense of computational efficiency. While we recognize the impressive accuracy of GAP, we contend that it is not well-suited for our large-scale MD simulations. We encourage the reader to consult previous GAP publications for a more thorough exploration of its performance.

3. Sample generation

Particular care was paid in generating the simulation cells, given that the structural and transport properties of amorphous materials can strongly depend on their synthesis or growth conditions [69–73]. Our primary objective was to study hydrogen and heat diffusion within c–Si/a–Si:H HJ. To this end, we prepared four c–Si simulation cells oriented along different low Miller index directions ([100], [110], [111], and [112]) with 3072–4608 atoms and side lengths varying from 7.6 to 8.1 nm, depending on the interatomic packing. Although standard c–Si/a–Si:H HJ are typically obtained by depositing intrinsic and doped a–Si:H layers on c–Si via PECVD [7], reproducing a realistic deposition process in

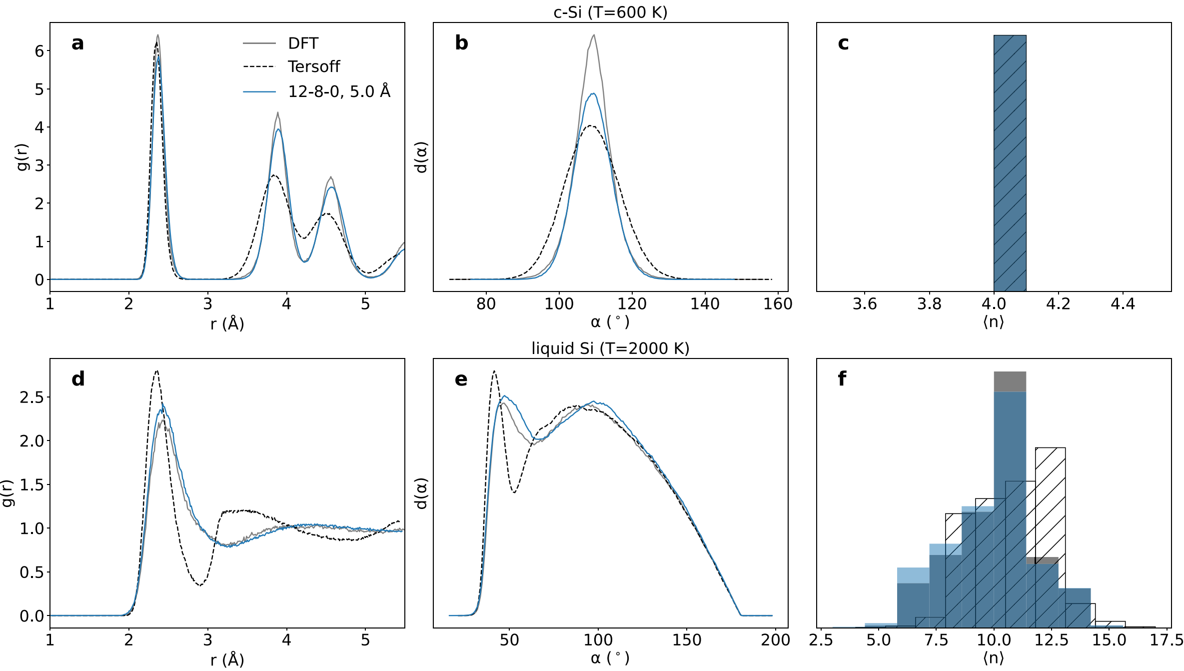

Figure 1. (a) and (d) Radial distribution functions for c–Si and a–Si, respectively. (b) and (e) Si–Si–Si angle distribution function for c–Si and a–Si respectively. (c) and (f) Distribution of average coordination numbers calculated within a 3.5 Å cut-off for c–Si and a–Si, respectively.

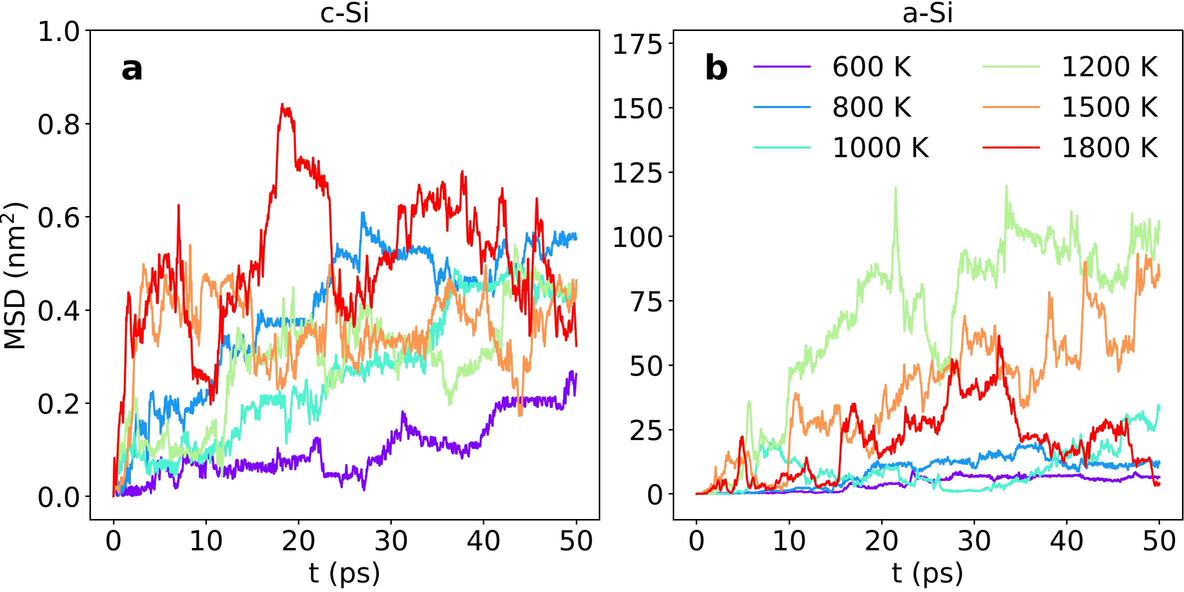

Figure 2. (a) and (b) Mean squared displacement as a function of temperature for an interstitial hydrogen atom in c–Si and a–Si, respectively.

an MD simulation would be impractical. Instead, we adopted a *quench-from-the-melt* protocol using a Nose–Hoover thermostat in the canonical ensemble: first, the oriented c-Si cell was heated from ambient temperature to 2000 K over 200 ps, then equilibrated at 2000 K for an additional 200 ps. Throughout this stage, the trajectory was carefully monitored to ensure the complete melting of the crystalline structure. Next, the temperature was rapidly reduced (over 50 ps) to 1800 K, placing the system in a supercooled regime below the melting point predicted by our potential (approximately 1800 K), yet still in a non-crystalline, liquid-like state. From this condition, the cell was cooled to 300 K at

Table 3. Amorphous silicon density as a function of the cooling rate γ_{cool} and of the crystalline orientation of the parent crystalline structure.

ρ_{aSi} (g cm^{-3})	1×10^{-1} K fs^{-1}	1×10^{-2} K fs^{-1}	1×10^{-3} K fs^{-1}	c–Si
[100]	2.413	2.370	2.352	2.299
[110]	2.432	2.402	2.390	
[111]	2.423	2.404	2.370	
[112]	2.422	2.417	2.394	
Expt.		2.288 [74]		2.330 [75]

three different cooling rates, $\gamma_{\mathrm{cool}} = 1 \times 10^{-1}$, 1×10^{-2}, and 1×10^{-3} K fs^{-1}, essentially running simulations between 15 ps and 1.5 ns. Following a previously established procedure for organic glasses [73], the configuration was periodically optimized at intervals of about 100 K and then allowed to relax for 20 ps at each temperature isothermal–isobaric (NpT) conditions. The simulation cell was free to relax along the direction defining the crystal orientation, while the two planar directions remained fixed. This protocol ensured that the system attained its equilibrium density without introducing any lattice mismatch when constructing the final heterostructure.

In table 3, we present the densities obtained from our simulations. While the c–Si density deviates by only about 1.2% from the experimental value, our amorphous structures end up somewhat denser than experimentally measured a–Si, which is approximately 1.8% less dense than c–Si. This discrepancy stems primarily from the large difference in timescales between experimental conditions and our computational protocol (cooling rates occur on the order of fractions of kelvin per femtoseconds). Consequently, the system is effectively 'arrested' at room temperature at a local configuration on the potential energy surface that differs from the true ground state for amorphous silicon. Indeed, we observe that reducing the cooling rate γ_{cool} yields progressively less dense amorphous samples, suggesting that extrapolating to experimentally relevant cooling rates would likely bring the computed densities in line with measured values. Following the quench procedure, we combined each crystalline and amorphous sample to form the heterostructures. The resulting systems were first optimized and then heated to 1000 K for 100 ps to minimize interface discontinuities, thus producing a smoother transition between the crystalline and amorphous regions. An example of these final heterostructures is shown in figure 3. The total length of the heterostructures ranges from approximately 14.7 to 16.1 nm.

Finally, we introduced hydrogen atoms into interstitial sites of the a–Si layer based on a distance-based criterion: any site with every Si–H distance of at least 1.2 Å was deemed suitable to accomodate an hydrogen atom. Using this approach, we populated the c–Si/a–Si heterostructures with 10, 100, or 500 hydrogen atoms, achieving a range of hydrogen concentrations between ~ 0.5 and ~ 10 atomic percent and similar to what investigated in previous computational studies [32] (typical experimental samples range between 5%–10%) [17, 76, 77]. The resulting structures were fully optimized before any other MD simulations.

4. Results and discussion

4.1. The Gibbs construction and the TBR

In bulk semiconductors heat conduction is mediated mainly by microscopic heat carriers (MHCs), which are phonons or other vibrational excitations (like locons, diffusions, propagons [78]) provided that we are respectively addressing a crystalline or amorphous material. In this context, the thermal transport properties are typically characterized by the thermal conductivity κ or its inverse, the thermal resistivity $\mathscr{R}$. Considering transport along one specific direction (e.g. z), the latter is usually determined via Fourier's law, $\partial T/\partial z = -\mathscr{R}J$, by explicitly computing the heat flux J temperature gradient $\partial T/\partial z$ under steady-state conditions. For completeness, in a system of thickness L_z and section area S, one can define the bulk thermal resistance as $R = \mathscr{R}L_z/S$. This framework is the basis of numerous non-equilibrium MDs (NEMDs) approaches [79, 80]. However, when an interface is present, the situation becomes more complex. Different thermal properties on each side of the interface can produce a sudden temperature discontinuity ΔT. Under steady-state conditions, this leads to the concept of TBR, often called Kapitza resistance [28, 81], which is phenomenologically expressed as $R^{\mathrm{TBR}} = \Delta T/J$. Although straightforward in principle, the evaluation of TBR in heterostructures is not trivial, as numerous details must be carefully addressed. Here, we determine the TBR of our heterostructures using the *Gibbs construction*, following a protocol derived by non-equilibrium thermodynamics concepts [82]. Within the Onsager formalism [83], one can derive that:

$$\frac{\partial}{\partial z}\left(\frac{1}{T}\right) = rJ \tag{5}$$

where J is the heat flux in the system, T is the temperature and r is the Onsager resistivity. Here we use the idea that the rate of entropy production within a material volume is generally expressed in the Onsager form $\sigma = \sum_i J_i X_i$ [83], meaning it is a sum of products between the ith flux J_i and its corresponding generalized force X_i. By assuming $X = \sum_i r_i J_i = rJ$ because no transport processes aside from heat flow are present, equation (5) indicates that the thermodynamic driving force for thermal transport is the gradient of an inverse temperature. The quantities r_i are known as Onsager resistivity coefficients, and in this context, they encompass all transport mechanisms that simplify to r under pure heat conduction [84, 85]. Extending this concept to an interface leads to the conclusion

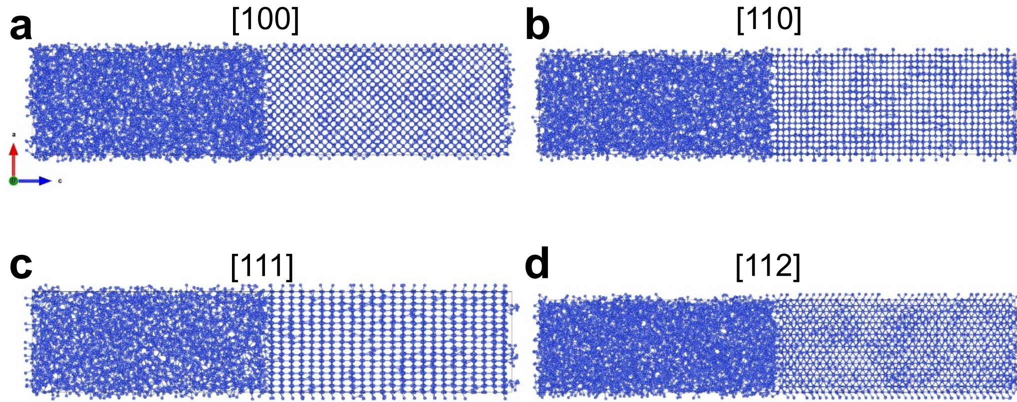

Figure 3. Side view of four prototypical heterostructures here investigated.

that the TBR can be viewed as a series of two Onsager resistances, which may be computed using the relation

$$R^{\mathrm{TBR}} = T_s^2\left(r^{\mathrm{left}} + r^{\mathrm{right}}\right) = T_s^2\frac{1}{J}\left(\frac{1}{T_{\mathrm{right}}} - \frac{1}{T_{\mathrm{left}}}\right) \quad (6)$$

where T_{left} and T_{right} refer to the temperatures directly at the boundaries of the interface region, and T_s denotes the interface temperature, taken as the average temperature in that same interfacial volume.

The Gibbs construction allows to identify the interface region and its boundaries. Specifically, one selects a suitable property $P(z)$ that assumes two distinct values in the bulk-like regions far from the interface. By plotting its variation along the direction normal to the interface, one can pinpoint the left and right boundaries (and thus the effective thickness of the interface) after choosing a criterion to define the interface as the region where $P(z)$ deviates by a chosen amount from the bulk values P_{left} and P_{right}. For example, for an interface between two semiconductors with mismatched lattices, $P(z)$ might be the interplanar spacing in the z direction. Alternatively, $P(z)$ could denote the local dopant concentration, a specific chemical species, or another structural defect. In the c–Si/a–Si:H HJ considered here, we employed the local average atomic coordination, a commonly used approach for crystalline/amorphous interfaces [82]. For this reason, we took special care to ensure that our ChIMES force field accurately reproduces the *ab initio* data regarding the average atomic coordination (see figure 1(f)).

Implementing this procedure involves performing the Gibbs construction for the interface, establishing a steady-state thermal conduction regime, and then determining the heat flux under those conditions. We enforced the steady-state condition within the NEMDs framework by assigning separate heat reservoirs at distinct temperatures to the left and right terminal regions of the simulation cell [80, 86]. The system is then aged in an MD run of sufficient duration for the temperature profile to become constant in time, indicating the achievement of steady state. To emulate realistic outdoor conditions, the a–Si side was thermostatted at 325, 350 and 400 K, whereas the opposite boundary was kept at 300 K. The thermostatted regions, corresponding to roughly 8% of the total system length, were coupled to a CSVR thermostat [87] while the remaining 'bulk' region was evolved in the microcanonical (*NVE*) ensemble to ensure the system reached steady state.

Once the system reached equilibrium, we monitored the work W^{hot} and W^{cold} done by the hot and cold thermostats, respectively, and calculated the heat fluxes as $J^{\mathrm{hot,cold}} = (1/S)(\partial W^{\mathrm{hot,cold}}/\partial t)$, where S represents the cross-sectional area of the simulation box. The steady-state condition is confirmed when J^{hot} and J^{cold} coincide within the numerical uncertainty [88, 89], thus removing the necessity for any explicit atomic-scale heat current formulation.

We report in figure 4(a) a representative outcome of a NEMD simulation: the two curves depict the work performed by the thermostats, while the black dashed lines mark the slopes $\partial W^{\mathrm{hot,cold}}/\partial t$ once the system attains steady state (which we define here as the point at which the work performed by the thermostats matches within 5%). In figure 4(b) we show the Gibbs construction: here, the average coordination number is employed to identify the left and right boundaries of the interfaces by pinpointing the z values where $\langle n_{\mathrm{coord.}}\rangle$ deviates by more than two standard deviations from the respective bulk-like reference values (depicted as horizontal black dashed lines). It is clear that, while c–Si is always characterized by $n_{\mathrm{coord.}} = 4$ and hence a very minimal variation is a fingerprint of a structural change, this quantity fluctuates considerably for a–Si, requiring particular care when identifying the interface. This analysis reveals that, although the interface is chemically well-defined, it retains a finite thickness of approximately 14 Å. Moreover, we observe that the interface region is asymmetric, largely situated within the c–Si region. As noted previously in the literature [82], the chemical interface does not necessarily coincide with the thermodynamic interface.

By utilizing this procedure, we calculated the TBR of our samples (table 4), a crucial parameter when examining c–Si/a–Si HJ. Indeed, not all the absorbed solar radiation is converted to electrical energy; a considerable fraction is dissipated as heat. The handling of this thermal load is vital, because excessive heat accumulation diminishes solar cell efficiency

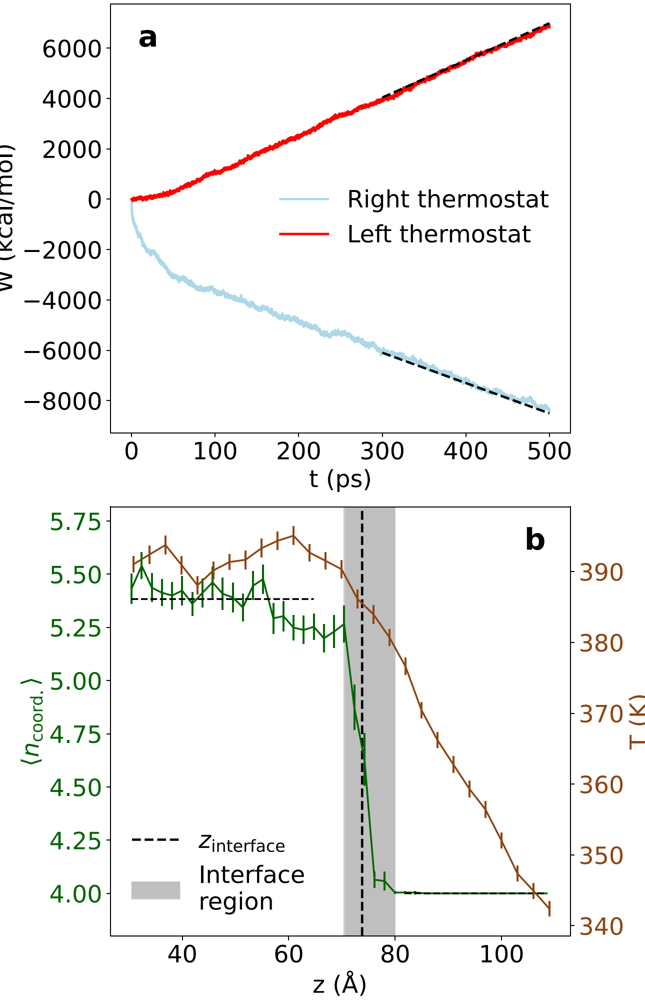

Figure 4. (a) Work performed by the two thermostats (red and blue curve) during a NEMD simulation. The dashed black lines represent the linear regime identifying the steady state, during which we calculated the heat fluxes as $(1/S)(\partial W^{\text{hot,cold}}/\partial t)$. (b) Gibbs construction for a [100]-oriented HJ calculated between $T = 400$ K and $T = 300$ K.

Table 4. Thermal boundary resistance (TBR in units m^2K/GW) and interface region widths w_{int} calculated at different temperatures, for different orientations, and for different cooling rates γ_{cool}.

	T (K)	10^{-1} K fs^{-1}	10^{-2} K fs^{-1}	10^{-3} K fs^{-1}
[100]	325	0.86	1.16	0.83
	350	0.41	1.32	2.39
	400	0.19	2.86	3.09
	w_{int} (Å)	11.3	13.4	7.6
[110]	325	1.85	1.69	1.91
	350	3.89	3.00	3.89
	400	5.53	5.02	5.67
	w_{int} (Å)	15.5	15.3	11.5
[111]	325	3.96	1.19	0.87
	350	2.70	2.55	1.47
	400	6.43	3.84	3.13
	w_{int} (Å)	17.5	10.0	7.5
[112]	325	3.46	4.08	3.03
	350	1.98	3.79	2.85
	400	3.85	4.95	5.78
	w_{int} (Å)	12.3	14.3	10.2

(e.g. through reductions in the open-circuit voltage and fill factor) and accelerates material degradation, thereby shortening device lifetimes. In a HJ cell, such as a c–Si/a–Si system, heat is generated within the bulk (due to carrier recombination) and at interfaces where different materials converge. If this thermal energy cannot pass efficiently across the HJ interface, it may lead to localized overheating, which can induce structural damage at the interface and degrade cell performance due to thermal stress or defect formation.

In most cases, TBR grows as the temperature increases from 325 K to 350 K and 400 K. The enhanced population of high-frequency MHCs results in greater scattering at the interface due to roughness, defects, or the amorphous–crystalline mismatch. When dealing with heat transport across solid-solid interfaces, the diffuse mismatch model (DMM) assumes that when phonons (and vibrational heat carriers in general) encounter disordered interfaces, they experience diffuse scattering: incident phonons interface lose their initial direction and phase. In fact, after interacting with the interface, they scatter into all allowed directions within either material, weighted by appropriate probability distributions [90, 91]. DMM is commonly used to study heat conduction across a variety of interfaces (e.g. metal–dielectric, semiconductor–semiconductor, and nanostructured interfaces). While the DMM would predict higher transmission probability, and thus reduced TBR [90, 92], lower cooling rates produce a 'better' amorphous network with localized structural disorder, hence enhancing MHCs scattering. Thus, in describing heat transport across c-Si/a-Si interfaces, the morphology of the amorphous region becomes a pivotal factor, effectively outweighing the role of temperature. In addition, the TBR values differ substantially across the various orientations. The [111] and [112] directions typically exhibit higher TBR values compared to [100] and [110] over certain temperature ranges and cooling rates, implying that the interface thermal resistance depends on the specific lattice structure and heat carriers transmission efficiency in different crystallographic planes. This indicates that heat carriers coupling across the interface varies with orientation due to differences in lattice mismatch and interfacial vibrational spectra. [100] and [111] directions are characterized by comparable dispersion relations, which can improve the overlap with the broad vibrational spectrum of the amorphous region, hence resulting in similar TBR. Their symmetry also supports more efficient transmission of transverse and longitudinal acoustic phonons, which constitute the main carriers for heat transport in c–Si. On the other hand, phonons in [110] have more complex dispersion relations, reducing the coupling with amorphous vibrational modes and hence leading to higher TBR [30, 90, 93]. Thus, although cleaving crystalline silicon along [100] produces smoother interfaces with fewer dangling bonds relative to [111], their vibrational transport properties both couple more effectively with a–Si compared to [110] and [112], which represents a less symmetric path. These observations align with the DMM, which predicts enhanced phonon transmission in orientations where lattice vibrations couple effectively across interfaces. In fact, prior studies [27–29] discussed the role of orientation-dependent phonon scattering in reducing interfacial thermal resistance: smoother interfaces and optimized vibrational mode overlap contribute to lower Kapitza resistance, as inferred from our results. Moreover, the a–Si quenching rate significantly impacts these quantities: for most orientations, faster quenching yields lower TBR at a given temperature, likely because the system becomes trapped in a local minimum of the potential energy surface differing from the "true" ground state. In contrast, slower cooling produces a more disordered amorphous region with enhanced MHCs scattering at the interface, resulting in higher TBR. In this context, it is worth pointing out that, while the width of the interface region shows a very weak dependence on γ_{cool} (with the lowest values observed for slower rates), its dependence on the crystalline orientations aligns with the observed TBR values: wider interfaces correspond to higher TBR (see table 4). This indicates that faster quenching rates might be ill-suited for accurately capturing the amorphous network and the morphology/thickness of the interfaces is ultimately that the controlling factor in defining TBR. The width dependence on crystallographic orientation is of particular interest, with the [111] plane consistently showing the narrowest interface region. This behavior is attributed to the different atomic packing and low surface energy of the [111] plane, which provide favorable conditions for efficient atomic arrangement and reduced structural disruption during cooling. The [111] orientation minimizes interface width due to its ability to promote stable, ordered growth at the atomic scale, making it less susceptible to disorder compared to other planes such as [110] and [112]. These characteristics of the [111] plane directly impact the thermal and transport properties of the c–Si/a–Si:H interface, as discussed below.

4.2. Hydrogen diffusion

In addition to the 'pristine' c–Si/a–Si HJ thermal properties, investigating hydrogen diffusion and its effect on heat diffusion is crucial because hydrogen plays a central role in determining the structural, electronic, and thermal properties of these cells. In fact, a–Si layers are used to passivate dangling bonds, significantly improving the electronic quality of the material by reducing defect states in the bandgap. Hydrogen diffusion can lead to changes in passivation over time, especially under thermal or light-induced stress, causing degradation in efficiency [15, 32].

The presence of hydrogen can modify the thermal characteristics of the HJ, potentially affecting heat dissipation under operating conditions and the stability of the device at high temperatures. Excessive heat accumulation can lead to thermal degradation of the cell, shortening both its service life and performance. Consequently, we targeted the samples quenched at $\gamma_{\mathrm{cool}} = 10^{-3}$ K fs^{-1}, introducing hydrogen into the amorphous interstitial sites at progressively increasing concentrations. We then placed the system in an out-of-equilibrium state via the approach-to-equilibrium MDs (AEMD) technique [94, 95]: the sample is ideally divided in half and the two regions are initialized at distinct temperatures ($T_{\mathrm{hot}} = 350$ K and $T_{\mathrm{cold}} = 300$ K) before being evolved in the *NVE* ensemble. This approach contrasts with the NEMD method utilized previously, as AEMD focuses on the transient regime rather than

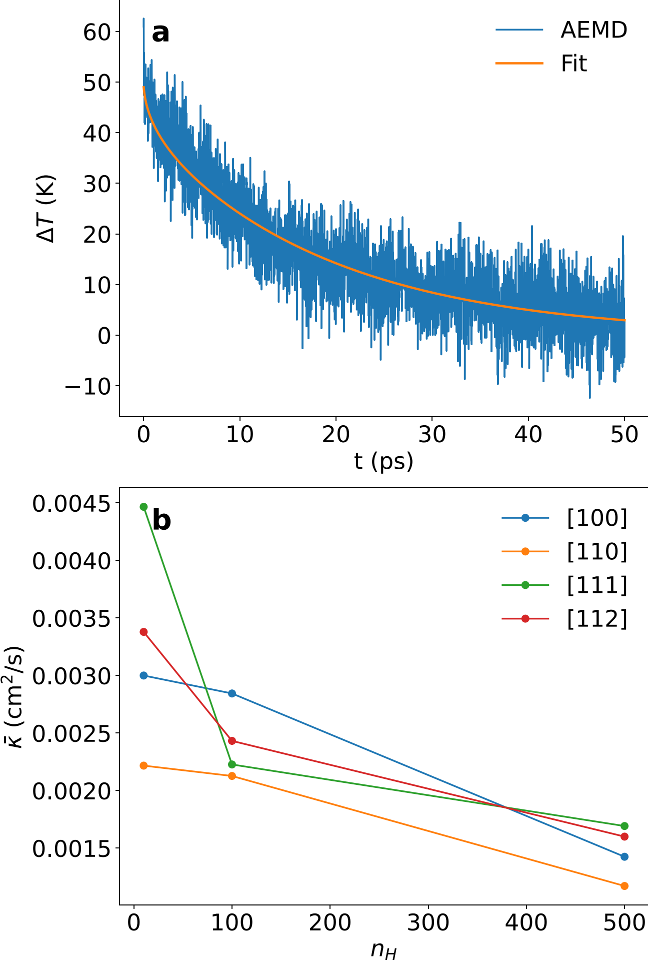

Figure 5. (a) Average temperature difference during an AEMD run for a [100] HJ and $n_\mathrm{H} = 100$ and the fit obtained with the solution of the 1D heat equation (equation (7)). (b) Calculated diffusivities for different crystal directions and hydrogen concentrations.

on the steady-state condition. The average temperature difference between the hot and cold regions was monitored during relaxation and fitted using the solution of the one-dimensional heat equation

$$\langle \Delta T(t)\rangle = \langle T_\mathrm{H}(t)\rangle - \langle T_\mathrm{C}(t)\rangle \propto \sum_{n=0}^{\infty} \frac{1}{2n+1} \mathrm{e}^{-\beta_n^2 \bar{\kappa} t} \tag{7}$$

with the thermal diffusivity $\bar{\kappa}$ acting as the fitting parameter (see previous works for further details [94, 95]). Although one could derive the thermal conductivity as $\kappa = c_v \rho \bar{\kappa}$—where c_v is the specific heat and ρ is the material density—we opt here to report only the thermal diffusivity for clarity, since obtaining c_v precisely and defining an average density for the composite system would be non-trivial. In what follows, we chose to thermalize the a–Si:H region at T_hot and the crystalline region at T_cold. Since the a–Si layer is directly illuminated due to its larger bandgap—which maximizes the solar cell efficiency—its local temperature may reach an operational range of 330–350 K, depending on specific conditions. [96, 97].

Figure 5 summarizes our results: the top panel displays the average temperature difference during the AEMD alongside its fit, while the bottom panel shows the extracted thermal diffusivity as a function of the crystalline orientation and the amount of hydrogen. We generally observe a decline in thermal diffusivity with increasing hydrogen concentration, because hydrogen introduces lattice perturbations that intensify MHCs scattering. It is worth noting that the degree of anisotropy in thermal diffusion differs significantly across the orientations when n_H increases from 10 to 100: we argue that the presence of more open structures in higher-index directions provides additional interstitial pathways, thus increasing the probability of hydrogen atoms crossing the interface between the amorphous and crystalline regions. Indeed, by examining the hydrogen MSD during the simulation (figure 6), one finds that for [111] it is greater than in the other orientations, which hints at higher hydrogen diffusivity and may enhance heat transport instead of hindering it. Moreover, [111] exhibits the lowest TBR values along with [100], indicating an advantage for efficient heat flow through the sample. These data are consistent with previously reported experimental works highlighting the critical role of crystallographic orientation in phonon transport and hydrogen diffusion. Experimental evidence suggests that silicon [111] orientation offers optimized heat transport and electron–hole pair generation, making it highly suitable for solar cell applications [6, 9]: heterostructures involving [111]-oriented crystalline silicon exhibit superior carrier mobility and reduced defect states, which align with our observations of improved hydrogen mobility and heat dissipation. Furthermore, hydrogen diffusion in silicon has been shown to depend strongly on crystallographic orientation [15]. The observed higher MSD along [111] confirms that open atomic pathways in the [111] direction provide less resistance to diffusing species, promoting faster diffusion rates. At larger n_H, the thermal diffusivity converges to near-identical values across all orientations. As the hydrogen fraction grows, the effect of crystallographic orientation on thermal conduction diminishes, suggesting that phonon scattering from hydrogen defects dominates over intrinsic lattice-dependent factors. As n_H rises, the MSD values among distinct orientations begin to merge, implying that in addition to disturbing the ‘ideal’ HJ structure and its inherent anisotropy, mutual scattering among hydrogen atoms becomes increasingly relevant, restricting hydrogen diffusion at the interface. This explains why the thermal diffusivities at high concentrations become smaller and nearly uniform.

Regarding thermal management in the device, the role of crystalline orientation is crucial. Larger thermal diffusivities are preferable to preserve performance and longevity, since they promote swift heat dispersion [98–100], minimizing thermal gradients that could trigger microcracks, delamination, or hydrogen migration from the a–Si:H layer. Reduced thermal strain extends the mechanical and electronic stability of the solar cell, while effective heat removal helps maintain operational efficiency. In our simulations, [110] direction tends to exhibit the worst thermal transport properties, whereas [111] can be considered advantageous for elevated thermal diffusivity and stability, especially at moderate hydrogen content.

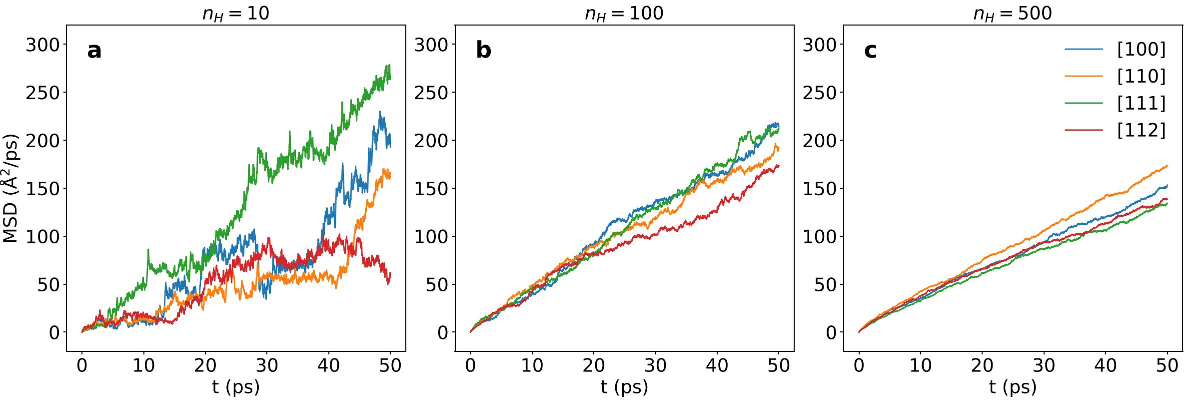

Figure 6. (a)–(c) Mean squared displacement obtained for different crystal directions and $n_\mathrm{H} = 10$, 100 and 500, respectively.

5. Conclusions

In this work, we combined the most advanced atomistic simulation strategies to deliver a comprehensive analysis of c–Si/a–Si heterostructures, evaluating their performance in terms of thermal transport and hydrogen incorporation. We employed a machine learning approach to develop an *ab initio*-level force field for Si–H interactions. The ChIMES-fitted force field captures both crystalline and amorphous silicon phases with excellent accuracy and offers higher computational efficiency compared to other non-linear machine-learned potentials (e.g. GAP). By constructing c–Si/a–Si heterostructures along various crystalline directions and exploring different quenching protocols for the amorphous component, we systematically characterized their TBR using NEMD and non-equilibrium thermodynamics. In particular, the Gibbs construction provided a detailed perspective on the interface region, treated as an independent thermodynamic subsystem. Next, we investigated the hydrogenated heterostructures to identify the optimal hydrogenation conditions for each crystalline orientation, aiming to enhance PV efficiency. Our findings indicate that moderate hydrogen concentrations ($\leqslant 10\%$) combined with specific crystallographic orientations (especially [111]) offer the most favorable conditions for maximizing device performance: moderate to high thermal diffusivity aids in rapid heat dissipation, mitigating thermal degradation, and ensuring sustained operation and reliability. Moreover, the cell thermal diffusivity should be carefully balanced with other design elements—such as cooling schemes—to achieve uniform heat distribution and minimize thermal stresses. Overall, these insights have the potential to guide the design and fabrication of c–Si/a–Si HJs for improved thermal management and superior performance in PV and other thermally sensitive applications.

Data availability statement

The data that support the findings of this study are openly available at the following URL/DOI: https://github.com/rdettori/cSi-aSiH_HS.

Acknowledgment

We acknowledge the financial support from 'e.INS—Ecosystem of Innovation for Next Generation Sardinia' - Project code ECS00000038, SPOKE 7 'Low carbon technologies for efficient energy systems', funded under the National Recovery and Resilience Plan (NRRP), Ministero dell'Università e della Ricerca (MUR); funded by the European Union—NextGenerationEU. We also acknowledge the CINECA award under the ISCRA initiative, for the availability of high-performance computing resources and support under Project IsCb5_HINTS HP10CEJ8V0.

ORCID iDs

Riccardo Dettori https://orcid.org/0000-0002-4678-1098
Claudio Melis https://orcid.org/0000-0002-5768-8403
Luciano Colombo https://orcid.org/0000-0001-5335-4652

References

[1] Green M A, Dunlop E D, Hohl-Ebinger J, Yoshita M, Kopidakis N and Hao X 2021 *Prog. Photovolt., Res. Appl.* **29** 657–67
[2] Yoshikawa K *et al* 2017 *Nat. Energy* **2** 32
[3] Fujiwara H and Kondo M 2007 *J. Appl. Phys.* **101** 75
[4] De Wolf S and Kondo M 2009 *J. Appl. Phys.* **105** 78
[5] Nunomura S, Tsutsumi T, Nakane K, Sato A, Sakata I and Hori M 2022 *Jpn. J. Appl. Phys.* **61** 056003
[6] De Wolf S, Descoeudres A, Holman Z C and Ballif C 2012 *Green* **2** 7–24
[7] Hayashi Y, Li D, Ogura A and Ohshita Y 2013 *IEEE J. Photovolt.* **3** 1149–55
[8] Luft W 1971 *IEEE Trans. Aerosp. Electron. Syst.* **AES-7** 332–9
[9] Battaglia C, de Nicolás S M, De Wolf S, Yin X, Zheng M, Ballif C and Javey A 2014 *Appl. Phys. Lett.* **104** 80
[10] Shockley W and Queisser H J 1961 *J. Appl. Phys.* **32** 510–9
[11] Kamioka T *et al* 2020 *Japan. J. Appl. Phys.* **59** SGGF06
[12] Garros X, Reimbold G, Cluzel J, Muñoz D and Ribeyron P-J 2011 *Microelectron. Eng.* **88** 1247–50
[13] Tucci M, Salurso E, Roca F and Palma F 2002 *Thin Solid Films* **403–404** 307–11

[14] Liu W, Zhang L, Cong S, Chen R, Wu Z, Meng F, Shi Q and Liu Z 2018 *Sol. Energy Mater. Sol. Cells* **174** 233–9
[15] Gotoh K, Wilde M, Kato S, Ogura S, Kurokawa Y, Fukutani K and Usami N 2019 *AIP Adv.* **9** 86
[16] A Luque and S Hegedus ed 2003 *Handbook of Photovoltaic Science and Engineering* (Wiley)
[17] Street R A 1991 *Hydrogenated Amorphous Silicon* (Cambridge University Press)
[18] Han D, Wang K and Yang L 1996 *J. Appl. Phys.* **80** 2475–82
[19] Qing Z, Fude L, Xianbo L and Guanglin K 1991 *J. Non-Cryst. Solids* **128** 86–90
[20] Pietruszko S and Jang J 2002 *Sol. Energy Mater. Sol. Cells* **71** 459–64
[21] Jagannathan B and Anderson W 1996 *Sol. Energy Mater. Sol. Cells* **44** 165–76
[22] Marsal L F, Pallarés J, Correig X, Calderer J and Alcubilla R 1996 *J. Appl. Phys.* **79** 8493–7
[23] Matsuura H, Okuno T, Okushi H and Tanaka K 1984 *J. Appl. Phys.* **55** 1012–9
[24] Nazarov A N, Vovk Y N, Lysenko V S, Turchanikov V I, Scryshevskii V A and Ashok S 2001 *J. Appl. Phys.* **89** 4422–8
[25] Song Y, Park M, Guliants E and Anderson W 2000 *Sol. Energy Mater. Sol. Cells* **64** 225–40
[26] Taguchi M, Maruyama E and Tanaka M 2008 *Jpn. J. Appl. Phys.* **47** 814
[27] Cahill D G, Ford W K, Goodson K E, Mahan G D, Majumdar A, Maris H J, Merlin R and Phillpot S R 2003 *J. Appl. Phys.* **93** 793–818
[28] Cahill D G *et al* 2014 *Appl. Phys. Rev.* **1** 011305
[29] Monachon C, Weber L and Dames C 2016 *Annu. Rev. Mater. Res.* **46** 433–63
[30] Pop E 2010 *Nano Res.* **3** 147–69
[31] Vincent J, Posa V R, Khouzam A, Logerais P-O, El Yaakoubi M and Labouret A 2023 *EPJ Photovolt.* **14** 25
[32] Diggs A *et al* 2023 *Commun. Mater.* **4** 6
[33] Rech B and Wagner H 1999 *Appl. Phys.* A **69** 155–67
[34] Gong C *et al* 2024 *Nat. Commun.* **15** 7
[35] Štich I, Car R and Parrinello M 1991 *Phys. Rev.* B **44** 11092–104
[36] Atta-Fynn R, Rathi S J, Arya H and Biswas P 2023 *J. Non-Cryst. Solids* **622** 122641
[37] Car R and Parrinello M 1988 *Phys. Rev. Lett.* **60** 204–7
[38] Drabold D A, Fedders P A, Sankey O F and Dow J D 1990 *Phys. Rev.* B **42** 5135–41
[39] Wang H, Zhang L, Han J and Weinan E 2018 *Comput. Phys. Commun.* **228** 178–84
[40] Cheng B, Engel E A, Behler J, Dellago C and Ceriotti M 2019 *Proc. Natl Acad. Sci. USA* **116** 1110–5
[41] Bartók A P, Kermode J, Bernstein N and Csányi G 2018 *Phys. Rev.* X **8** 041048
[42] Zhou G, Lubbers N, Barros K, Tretiak S and Nebgen B 2022 *Proc. Natl Acad. Sci. USA* **19** e2120333119
[43] Lindsey R K, Fried L E and Goldman N 2017 *J. Chem. Theory Comput.* **13** 6222–9
[44] Lindsey R K, Fried L E, Goldman N and Bastea S 2020 *J. Chem. Phys.* **153** 134117
[45] Lindsey R K, Goldman N, Fried L E and Bastea S 2020 *J. Chem. Phys.* **153** 054103
[46] Koziol L, Fried L E and Goldman N 2017 *J. Chem. Theory Comput.* **13** 135–46
[47] Lindsey R K, Fried L E and Goldman N 2019 *J. Chem. Theory Comput.* **15** 436–47
[48] Armstrong M R, Lindsey R K, Goldman N, Nielsen M H, Stavrou E, Fried L E, Zaug J M and Bastea S 2020 *Nat. Commun.* **11** 353
[49] Pham C H, Lindsey R K, Fried L E and Goldman N 2021 *J. Chem. Phys.* **153** 224102
[50] Goldman N, Fried L E, Lindsey R K, Pham C H and Dettori R 2023 *J. Chem. Phys.* **158** 16
[51] Goldman N *et al* 2021 *J. Chem. Theory Comput.* **17** 4435–48
[52] Wang Y, Shepler B C, Braams B J and Bowman J M 2009 *J. Chem. Phys.* **131** 054511
[53] Wang Y, Huang X, Shepler B C, Braams B J and Bowman J M 2011 *J. Chem. Phys.* **134** 094509
[54] Tersoff J 1988 *Phys. Rev. Lett.* **61** 2879
[55] Kresse G and Furthmüller J 1996 *Phys. Rev.* B **54** 11169–86
[56] Blöchl P E 1994 *Phys. Rev.* B **50** 17953–79
[57] Kresse G and Joubert D 1999 *Phys. Rev.* B **59** 1758–75
[58] Perdew J P, Burke K and Enzerhof M 1996 *Phys. Rev. Lett.* **77** 3865–8
[59] Mermin N D 1965 *Phys. Rev.* **137** 1441–3
[60] Monkhorst H J and Pack J D 1976 *Phys. Rev.* B **13** 5188–92
[61] Bartók A P, Kermode J, Bernstein N and Csányi G 2018 *Phys. Rev.* X **8** 48
[62] Efron B, Hastie T, Johnstone I and Tibshirani R 2004 *Ann. Stat.* **32** 407–99
[63] Friedman J, Hastie T and Tibshirani R 2010 *J. Stat. Softw.* **33** 1
[64] Tibshirani R 1996 *J. R. Stat. Soc.* B **58** 267–88
[65] Thompson A P *et al* 2022 *Comput. Phys. Commun.* **271** 108171
[66] Panzarini G and Colombo L 1994 *Phys. Rev. Lett.* **73** 1636–9
[67] Buda F, Chiarotti G L, Car R and Parrinello M 1989 *Phys. Rev. Lett.* **63** 294–7
[68] Unruh D, Meidanshahi R V, Goodnick S M, Csányi G and Zimányi G T 2022 *Phys. Rev. Mater.* **6** 3
[69] Li W and Ando Y 2019 *J. Chem. Phys.* **151** 52
[70] Van Hoang V 2007 *Phys. Status Solidi* b **244** 1280–7
[71] Van Hoang V 2015 *Physica* B **456** 50–56
[72] Ráfols-Ribé J *et al* 2018 *Phys. Rev. Mater.* **2** 3
[73] Rodríguez-López M *et al* 2024 *J. Mater. Chem.* **12** 18111–20
[74] Custer J S, Thompson M O, Jacobson D C, Poate J M, Roorda S, Sinke W C and Spaepen F 1994 *Appl. Phys. Lett.* **64** 437–9
[75] McGuire G F 1988 *Semiconductor Materials and Process Technology Handbook* (William Andrew Publishing)
[76] Staebler D L and Wronski C R 1980 *J. Appl. Phys.* **51** 3262–8
[77] Guha S 1997 *Curr. Opin. Solid State Mater. Sci.* **2** 425–9
[78] Allen P B, Feldman J L, Fabian J and Wooten F 1999 *Phil. Mag.* B **79** 1715–31
[79] Jund P and Jullie R 1999 *Phys. Rev.* B **59** 13707–11
[80] Sellan D, Landry E S, Turney J E, McGaughey A J H and Amon C H 2010 *Phys. Rev.* B **81** 214305
[81] Pollack G L 1969 *Rev. Mod. Phys.* **41** 48–81
[82] Dettori R, Melis C, Cartoixá X, Rurali R and Colombo L 2016 *Adv. Phys.* X **1** 246–61
[83] Kjelstrup S and Bedeaux D 2011 *Thermodynamic Relations for Heterogeneous Systems* (World Scientific)
[84] Cappai A, Dettori R, Marini F, Melis C and Colombo L 2024 *Appl. Phys. Lett.* **124** 44
[85] Cappai A, Colombo L and Melis C 2024 *Adv. Theory Simul.* **7** 49
[86] He Y, Savić I, Donadio D and Galli G 2012 *Phys. Chem. Chem. Phys.* **14** 16209–22
[87] Bussi G, Donadio D and Parrinello M 2007 *J. Chem. Phys.* **126** 20
[88] Melis C, Barbarino G and Colombo L 2015 *Phys. Rev.* B **92** 245408
[89] Dettori R, Melis C, Rurali R and Colombo L 2016 *J. Appl. Phys.* **119** 42
[90] Swartz E T and Pohl R O 1989 *Rev. Mod. Phys.* **61** 605–68
[91] Peterson R B 1994 *J. Heat Transfer* **116** 815–22
[92] Little W A 1959 *Can. J. Phys.* **37** 334–49

[93] Lyeo H-K and Cahill D G 2006 *Phys. Rev.* B **73** 1
[94] Melis C, Dettori R, Vandermeulen S and Colombo L 2014 *Eur. Phys. J.* B **87** 9
[95] Cappai A, Melis C, Colombo L and Dettori R 2024 *Molecular Dynamics Simulations of Thermal Transport in Solid State Systems* (Elsevier) pp 804–20
[96] Riesen Y, Stuckelberger M, Haug F-J, Ballif C and Wyrsch N 2016 *J. Appl. Phys.* **119** 92
[97] Ghannam M Y 2023 Temperature dependence of light-enhanced series resistance, fill factor and efficiency of a-Si:H/c-Si heterojunction solar cells *SILICONPV 2022, The 12th Int. Conf. on Crystalline Silicon Photovoltaics* vol 2826 (AIP Publishing) p 040001
[98] Shaker L M, Al-Amiery A A, Hanoon M M, Al-Azzawi W K and Kadhum A A H 2024 *Sustain. Energy Res.* **11** 8
[99] Gaitho F, Ndiritu F, Muriithi P, Ngumbu R and Ngareh J 2009 *Sol. Energy* **83** 1290–3
[100] Huang X, Lin Y, Alva G and Fang G 2017 *Sol. Energy Mater. Sol. Cells* **170** 68–76